Optical imaging of post-embryonic zebrafish using multi orientation -raster scan optoacoustic mesoscopy

Murad Omar[1,2,+*], Johannes Rebling[1,2*], Kai Wicker[3*], Tobias Schmitt-Manderbach[3], Mathias Schwarz[1,2], Jérôme Gateau[4], Hérnan Lopez-Schier[5], Timo Mappes[6], and Vasilis Ntziachristos[1,2,+]

[1]Chair for Biological Imaging, Technische Universität München, Ismaningerstr. 22, 81675, München, Germany

[2]Institute for Biological and Medical Imaging, Helmholtz Zentrum München, Ingolstädter Landstr. 1, 85764, Neuherberg, Germany

[3]Carl Zeiss AG, Corporate Research and Technology, Carl Zeiss Promenade 10, 07745 Jena, Germany

[4]ESPCI ParisTech, PSL Research University, CNRS, INSERM, Institut Langevin, 1 rue de Jussieu, 75005, Paris, France

[5]Research unit sensory biology and organogenesis, Helmholtz Zentrum München, Ingolstädter Landstr. 1, 85764, Neuherberg, Germany

[6]Carl Zeiss Vision International GmbH, Technology & Innovation, Turnstr. 27, 73430 Aalen, Germany

*These authors contributed equally to this work

[+]Correspondence should be addressed to: murad.omar@tum.de, v.ntziachristos@tum.de

Abstract

Whole-body optical imaging of post-embryonic stage model organisms is a challenging and long sought-after goal. It requires a combination of high-resolution performance and high-penetration depth. Optoacoustic (photoacoustic) mesoscopy holds great promise, as it penetrates deeper than optical and optoacoustic microscopy, while providing high spatial resolution. However, optoacoustic mesoscopic techniques, only offer partial visibility of oriented structures, such as blood vessels, due to limited angular detection aperture or employ ultrasound frequencies that yield insufficient resolution. We introduce 360-degree multi-orientation (multi-projection) raster scan optoacoustic mesoscopy (MORSOM) based on detecting ultra-wide frequency bandwidth (up to 160 MHz) and weighted de-convolution to synthetically enlarge the angular aperture. We demonstrate unprecedented isotropic in-plane resolution at the 9-17 micron range and improved signal to noise ratio (SNR) in phantoms and opaque 21-day-old zebrafish. We find that MORSOM performance defines a new operational specification for optoacoustic mesoscopy of adult organisms with possible applications in developmental biology of adulthood and aging.

Keywords

Optoacoustics, Photoacoustics, Mesoscopy, Multiview, Deconvolution, Development.

Introduction

Model organisms such as Zebrafish and Drosophila Melanogaster are widely used in developmental biology and experimental genetics[1,2]. Although they are important biological models, optical imaging in such samples is most often limited to the embryonic stage due to optical diffusion[3]. In this embryonic stage, samples are typically small in size and virtually transparent so that they can be imaged *in-vivo* using single-plane illumination microscopy (SPIM)[3]. Optical microscopy of larger specimen requires optical clearing using chemicals that are toxic and not suited for *in-vivo* imaging. Alternative methods that enable intravital microscopy include confocal, multi-photon[4,5] or optoacoustic microscopy[6] techniques which are nevertheless limited to depths of the order of a few hundred microns due to the physical limits of focusing a light beam deep within highly scattering media[4].

Imaging of larger opaque biological specimen is important for observing biological processes *in-vivo* and longitudinally[1,2,7]. Imaging beyond the embryonic stage can allow observations of processes associated with development into adulthood and aging. Raster scan optoacoustic mesoscopy (RSOM)[8,9] has been recently introduced for imaging model organisms and disease development, such as tumor growth in mice[10]. The method has shown to image samples at depths of up to 5 mm, with a resolution of 4-20 μm[8,9], bridging imaging ability between microscopic and macroscopic imaging, such as multispectral optoacoustic tomography[11-13]. However, RSOM of model organisms, such as zebrafish, is limited due to the low numerical aperture ($N.A.$) of the ultrasonic detectors used, typically ~60 degrees. Consequently, RSOM exhibits highly anisotropic resolution in the *xy*-plane which only

partially detects directional objects[8,14] and may miss certain structures (see figure 1S in supplementary material).

Herein, we introduce multi-orientation RSOM (MORSOM), a technique that collects RSOM projections over 360 degree angles in analogy to X-ray CT. In contrast to multi-view optoacoustic microscopy[6], which utilizes focused light beams and image formation based on optical-diffraction, MORSOM utilizes broad-field illumination and forms images based on the ultrasonic-diffraction limit. For this reason, a particular MORSOM feature is the use of ultra-wideband detection (up to 160 MHz) to achieve high-resolution and a broad coverage of spatial frequencies, necessary for capturing high quality images. This feature is in contradistinction with optoacoustic mesoscopy studies performed with narrow-band, high-element-pitch linear array detectors[15,16]. Finally, image reconstruction schemes are necessary to offer optimal combination of the MORSOM projections collected.

We hypothesized that MORSOM could yield unprecedented imaging performance over RSOM while allowing penetration depths that are superior to optical resolution microscopy[6]. To investigate this hypothesis we developed a MORSOM experimental setup and investigated the performance with phantoms and 21 days post fertilization (dpf) old zebrafish, i.e., a target tissue that has not been shown possible to image with SPIM[17], or optical resolution optoacoustic microscopy[6,10,18]. We further investigated the relative performance of MORSOM over conventional RSOM.

Materials and methods

System design

We present the experimental setup in figure 1. The setup was designed to accommodate imaging of model organisms. The sample is positioned along the axis of rotation, the *z*-axis, by placing it on a rotation stage. The spherically-focused detector was scanned in the *xz*-plane, using two linear stages (M683 and M404-2PD, Physik Instrumente GmbH, Karlsruhe, Germany). We scan the sample in an alternating continuous-discrete manner, where the *x*-stage is continuously moved, while the *z*-stage is moved step-wise from one line to the next one to acquire each orientation. At the end of every *xz*-scan, the sample is rotated, using a rotational stage (RS-40, PI-MICOS, Karlsruhe, Germany), over 360 degrees.

Optical excitation was based on 532 nm, 1 ns pulse width, 2 kHz repetition rate laser (Bright Solutions SRL, Pavia, Italy) emitting 1 mJ/pulse. Light was directed to the specimen via fibers (Ceram Optec GmbH, Bonn, Germany), achieving coupling efficiency of ~30%. The light intensity delivered to the sample was ~0.32 mJ/cm^2, i.e. approximately two orders of magnitude less than the ANSI limit for biological samples. To generate a homogeneous illumination at the sample, we placed four fiber arms 90° apart and at a distance of 14.5 mm from the axis of rotation (see figure 2S).

Detection was based on custom-made single element detectors with ultra-wideband detection. A detector with nominal central frequency of 50 MHz attained a focal distance of 3 mm, numerical aperture $N.A. \approx 0.5$ and ultra-wide band acoustical -6 dB-bandwidth of 23-115 MHz (see figure 3S.a). A second detector with nominal central frequency of 100 MHz attained acoustical -6 dB-bandwidth of 20-180 MHz, focal distance of 1.65 mm and numerical aperture $N.A. \approx 0.45$. The detectors were connected to a 63 dB low-noise amplifier (AU-1291, Miteq Inc.,

Hauppauge, New York, USA). Signals were digitized using a fast data acquisition card (ADQ412-3G, SP-Devices, Linköping, Sweden) at 900 MS/s, and 12 bit resolution. The minimum angular step size ($\Delta\phi_{min}$), necessary to ensure that all the optoacoustic waves generated within the sample and in the xy-plane are captured, is given by the angle of acceptance of the detector. Consequently, we chose a rotation step of $\Delta\phi = 20°$ for enhanced SNR, and for implementing the same number of rotation steps when comparing the 50 MHz and the 100 MHz data, see figure 1S. This choice leads to $N_\phi = 18$ orientations. Detector scanning was performed along the *xz*-plane with 20 μm step size for the 50 MHz case, and 10 μm step size for the 100 MHz case.

Samples and preparation

We characterized the MORSOM imaging performance in terms of resolution, SNR and overall image quality using a phantom consisting of 10 μm spheres randomly dispersed in agar gel and juvenile zebrafish, at 21 days post fertilization (dpf). At 21 dpf zebrafish have a length of ~10 mm and diameters ranging from 1.2 to 2 mm (see figure 4S in the supplementary material). These dimensions are not accessible by optical, or optoacoustic microscopy techniques, such as SPIM[17] or multiview optical resolution photoacoustic microscopy[6,18,19], and correspond to dimensions for which optoacoustic mesoscopy may be ideally suited. Zebrafish were embedded in low melting agar (Sigma-Aldrich) and imaged *ex-vivo*, consistent with current regulations and processes allowed by the Government of Upper Bavaria for adult fish. The agar was mixed with ~10 μm diameter black microspheres (black polystyrene microspheres, Polybead, Polysciences Inc., Warrington, Pennsylvania) which we employed as fiducial markers to confirm the exact alignment of the different

RSOM projections onto the common MORSOM image reconstruction scheme. The zebrafish / agar specimen was mounted on a syringe, as previously described for SPIM[20] and placed in a water bath for acoustic coupling.

Reconstruction and de-convolution

Planar raster scans were reconstructed separately in the local coordinates of the scan using three-dimensional beamforming with dynamic aperture[8,9]. For accelerated performance we parallelized the reconstruction on a graphical processing unit. Image grids were composed of 20 × 5 × 20 μm^3 voxels.

Alignment of the individual projections

After reconstruction in the local coordinates (x', y', z'), we transform the three-dimensional reconstructions to the global coordinates (x, y, z), with voxel sizes of 5 x 5 × 20 μm^3, through a linear transformation including two translations and a rotation. For example, the image $I_m(x', y', z')$ from the m^{th} orientation, is transformed to the global coordinates as: $I_m(x, y, z) = T\{I_m(x', y', z'), \Delta x, \Delta y, \phi_m\}$, where ϕ_m is the angle of rotation and $(\Delta x, \Delta y)$ is a shift vector necessary to account for location of the rotation axis in the reconstructed volume. We only approximately knew the vector coordinates from the mechanical positioning, thus we performed a calibration procedure to determine the exact vector coordinates. This calibration procedure was based on the reconstruction of the previously embedded 10 μm microspheres, our feducial markers. We selected the vector coordinates on the criterion of maximum brightness, which corresponds to the most coherent sum from all the orientations. To improve the co-registration of the individual orientations, we performed a fine calibration using cross-correlations in the spatial Fourier domain. This fine calibration is an important step, as it allows sub-pixel calculation of the vector coordinates, and

corrects for differences in the shift vectors between different orientations, as well as for the tilt of the scanning plane.

Weighted sum and Wiener filtering

The simplest way to combine the images from the individual views ($I_m(x,y;z_i)$) into a final image ($I(x,y;z_i)$) would be a simple summation: $I(x,y;z_i) = \sum_{m=1}^{N_\phi} I_m(x,y;z_i)$, or in spatial frequency space: $\tilde{I}(k_x,k_y;z_i) = \sum_{m=1}^{N_\phi} \tilde{I}_m(k_x,k_y;z_i)$. This is shown for a bead in figure 2.d. This reconstruction is not ideal however, as it does not take into account the different optical transfer functions (OTF, the Fourier transform of the point spread function or the PSF) $OTF_m(k_x,k_y)$ of the individual views (figure 2.b):

$$\tilde{I}_m(k_x,k_y;z_i) = \tilde{S}(k_x,k_y;z_i) \times OTF_m(k_x,k_y), \quad (1)$$

where: $\tilde{S}(k_x,k_y;z_i)$ is the 2D frequency representation of the sample absorber distribution for the slice $z = z_i$. At any given spatial frequency, both amplitude and phase can vary between the OTFs of the different views. This influences the result of the summation in two ways: Firstly, for varying phases, the above sum over all OTFs will have a lower value than it would have if all phases were equal, leading to a reduced SNR. Secondly, at spatial frequencies where the amplitude of a view's OTF is low, this view cannot contribute much information to the sum image, while it will still add its noise components, again leading to reduced SNR.

Thus, to reduce the noise propagated from one view to the neighboring ones during reconstruction, we calculate a *weighted* sum in the Fourier space[21]:

$$\tilde{I}_{WS}(k_x,k_y;z_i) = \sum_{m=1}^{N_\phi} \tilde{w}_m(k_x,k_y)\tilde{I}_m(k_x,k_y;z_i)$$

$$= \sum_{m=1}^{N_\phi} \tilde{w}_m(k_x, k_y)\tilde{S}(k_x, k_y; z_i)OTF_m(k_x, k_y), \quad (2)$$

where: $\tilde{w}_m(k_x, k_y)$ are view dependent weight maps. These weight maps are chosen as the complex conjugate of the view's OTFs: $\tilde{w}_m(k_x, k_y) = OTF_m^*(k_x, k_y)$. This has two effects: Firstly, it compensates any unwanted phase effects in the OTFs:

$$\tilde{I}_{WS}(k_x, k_y; z_i) = \sum_{m=1}^{N_\phi} OTF_m^*(k_x, k_y)\tilde{I}_m(k_x, k_y; z_i)$$

$$= \sum_{m=1}^{N_\phi} \tilde{S}_m(k_x, k_y; z_i)\left|OTF_m(k_x, k_y)\right|^2. \quad (3)$$

Secondly, it weights a view's contribution at a certain frequency according to the amplitude of its OTF. Views with low transfer strengths (i.e. bad SNR) will therefore contribute very little, whereas views with strong transfer strengths (i.e. good SNR) contribute strongly. Choosing weight maps in this manner combines the information contained in the different view images in an SNR-optimized way. It can also compensate for phase shifts due to the electric impulse response of the detector.

This recombined image corresponds to the sample slice being imaged with an effective OTF:

$$\tilde{I}_{WS}(k_x, k_y; z_i) = \tilde{S}_m(k_x, k_y; z_i)OTF_{WS}(k_x, k_y), \quad (4)$$

with $OTF_{WS}(k_x, k_y) = \sum_{m=1}^{N_\phi}\left|OTF_m(k_x, k_y)\right|^2$. The result of this process is shown for a bead in figure 2.e.

Finally, the resulting image can be further enhanced by applying a generalized Wiener filter[21,22], which leads to a reduction of side lobes (figure 2.f):

$$\tilde{I}_{Wiener}(k_x, k_y; z_i) = \frac{\tilde{I}_{WS}(k_x,k_y;z_i)\cdot OTF_{WS}^*(k_x,k_y)}{\left|OTF_{WS}(k_x,k_y)\right|^2+\omega^2}. \quad (5)$$

In the actual reconstructions, we chose the Wiener factor ω empirically as 10^{-3}. The OTF was calculated as a 2D Fourier transform of the PSF, which was determined experimentally as described in the supplementary material.

Results and discussion

MORSOM images from a phantom of 10 μm black microspheres, suspended in agar obtained with 18 RSOM projections (figure 2) characterized the imaging performance. Figure 2.a shows a single projection image (RSOM) revealing the point spread function (PSF) for the 50 MHz detector. Deconvolution of RSOM images with the Optical Transfer Function (OTF) (figure 2.b) results in noise suppression and phase correction (figure 2.c) compared to an original RSOM projection (figure 2.a). Figure 2.d shows a MORSOM image resulting from directly summing the different RSOM projections after cross-correlation based sub-pixel co-registration, which enhances the SNR by 6 dB. The use of a weighted sum of the different orientations (projections) suppresses imaging artifacts (figure 2.e) over figure 2.d. Finally, the application of the Wiener filter (figure 2.f) leads to a further suppression of imaging artifacts compared to both figure 2.d and figure 2.e, evident in the reduction of negative values, and streak artifacts. Using Wiener filter further enhances the SNR by 9 dB over non weighted MORSOM reconstruction, for a total 15 dB improvement in SNR in comparison to the performance of single-projection RSOM.

Theoretical calculations predicted[23,24] (see supplementary material) the resolution of the 50 MHz MORSOM system to be 16 μm in the xy-plane, and 43 μm along the axis of rotation (the z-axis). Cross sections taken through one of the microspheres appearing on figure 3S.b after reconstruction revealed that the resolution along the z-axis (δ_z) equaled 44 μm (full width at half maximum ($FWHM$)),

while the resolution within the xy-plane (δ_{xy}) improved by a factor of ~3 along the y-axis over single projection RSOM to ~17 μm. The corresponding in-plane resolution for 100 MHz MORSOM was approximately 10 μm.

Figure 3 presents maximum intensity projection (MIP) images of MORSOM and RSOM from the 21 dpf zebrafish at 23-115 MHz bandwidth (50Mhz detector). As with the microsphere measurements, we notice the improved SNR of the MORSOM images in comparison to RSOM images. Figure 3.a shows a lateral image of the zebrafish imaged with MORSOM, while figure 3.b shows the same lateral image acquired using RSOM. A comparison of the two images reveals enhancements in terms of contrast and SNR for MORSOM over RSOM. Marked differences are particularly evident at the dorsal side of the fish (figures 3.c and 3.d), i.e. at the fish sides not facing the detector. The differences between MORSOM and RSOM may be better understood by observing cross sections through the fish (axial images figures 3.e and 3.f). MORSOM reveals anatomical features with unparalleled clarity compared to single orientation images acquired with RSOM. Structures such as the boundary of the zebrafish, and the boundary of some internal organs are well visualized in MORSOM but fail to reconstruct in RSOM, the latter revealing almost none of the internal organs. We can pinpoint several examples of enhancement; for example, the labels 1 and 3 point to the boundary of internal organs inside the zebrafish, this boundary is clearly visible in figure 3.e, while it is incomplete in figure 3.f. Another example, are labels 5 and 6, these two labels point to structures that are visible only in figure 3.e, i.e. in MORSOM. The cross-sections generated from MORSOM correspond well with the distribution of structures inside the zebrafish[25]. For example; the eyes, the pigmentations, the fins, the spinal cord, and the pharyngeal cartilages are clearly seen.

A comparison of MORSOM imaging at 50 MHz and 100 MHz (figure 4) revealed enhanced resolution and better differentiation of anatomical features when using the higher frequency detector. Figures 4.a and 4.b show MIPs taken from the dorsal side of a zebrafish using the 50 MHz and the 100 MHz detectors respectively. The lateral fish sides imaged by the 50 MHz and 100MHz detectors are shown in figures 4.c and 4.d respectively and cross-sections taken with the 2 detectors in figures 4.e and 4.f. The images confirm the enhanced resolution achieved with the 100 MHz detector (acoustic bandwidth 20-180 MHz) to the 50 MHz, 92 MHz bandwidth case. On the other hand, the 50 MHz detector yields images with higher signal to noise ratio, thus higher sensitivity to weak absorbers. Due to the increased SNR and coarser step, 50 MHz imaging required 20 minutes of acquisition time vs. 80 minutes for the 100 MHz system. Therefore, the choice between the 50 MHz detector and the 100 MHz detector imposes a trade-off between sensitivity, scanning time, and resolution. We expect the 160 MHz-bandwidth detection to be better suited for imaging finer anatomical features, i.e. specimen where higher resolution is necessary. Conversely, the 92 MHz bandwidth detector may be more appropriate for resolving spectral features with higher SNR, when multi-wavelength imaging is implemented.

Although single band images were shown herein, multi-frequency-band images could be generated for higher fidelity and better representation of low and high spatial frequencies[26]. This can be achieved by separately processing frequency sub-bands from the ultra-wide ultrasound frequency spectrum collected.

Conclusions

We combined optoacoustic imaging over 360-degree projections with ultra-wide band detection ranging from 92 MHz to 160 MHz, to achieve high performing optoacoustic mesoscopy. The method synthetically captures the optoacoustic waves propagating at multiple projections normal to the axis of rotation. The use of multi-view approaches is common in many imaging modalities, including optical resolution optoacoustic microscopy[6], in selective plane illumination microscopy[17], optoacoustic macroscopy using linear arrays[27,28], or X-ray CT. However, MORSOM comes with unique features leading to true mesoscopic optoacoustic imaging performance not previously demonstrated. MORSOM offers for the first time ultra-broadband multi-orientation mesoscopy appropriate for imaging model organisms. High imaging performance is achieved using a particular single-element ultra-wide-band high-frequency detector design that enables multi-orientation scanning over a 160 MHz band for the 100 MHz central frequency detector and a ~92 MHz band for the 50 MHz central frequency detector. Ultra-wideband detection is necessary in order to resolve slow varying and fast varying spatial contributions, resulting in resolution and overall image quality not enabled at narrower bands. Combined with a complete 360-degrees angular coverage, MORSOM yielded high fidelity images of opaque biological tissues not accessible by optical and optoacoustic microscopy methods.

We chose single element detectors since detector arrays may achieve only up to 35 MHz bandwidths and have less preferential focusing characteristics. Therefore, MORSOM capitalizes on collecting a uniquely rich and spatially precise data set, which we combined with a novel image reconstruction implementation to enable higher SNR and higher and more isotropic in-plane resolution compared to RSOM.

MORSOM-50 zebrafish images exhibited higher contrast, richer anatomical detail and an improved SNR of ~15 dB over RSOM, as evident on figure 3.e vs. figure 3.f. MORSOM-100 images specimen with higher resolution (~ 9 microns vs. 17 microns) but with reduced SNR. Overall, MORSOM visualized diameters of up to 2 mm, much deeper than what is allowed by SPIM or multiview optical resolution microscopy[6]; the latter operating on optical diffraction resolution using focused light beams and much higher resolution compared to optoacoustic mesoscopy implemented with linear arrays[15,16]. Possibly, the combination of advanced ultrasound detection techniques, including annular detector arrays[29], can improve the SNR and focusing ability of the detector employed leading to improved lateral resolution over the current implementation and an extended imaging depth. Nevertheless, sound attenuation, especially in the higher frequencies, will ultimately limit the penetration that can be achieved while maintaining high resolution.

A current limitation of MORSOM in comparison to RSOM is the scan duration, as several RSOM scans should be performed. A MORSOM scan at 50 MHz central frequency may take up to 20 minutes (up to 80 minutes for 100 MHz). This time scale does not limit the study of slow developmental processes happening within juvenile, and adult zebrafish, occuring on a time scale of hours to days, e.g. organ development, growth of the vascular network, or changes to the neural network. Nevertheless, shorter time scales would be important for capturing faster phenomena and increasing throughput. The MORSOM scan-times could be reduced by an optimized combination of N_ϕ and N_x, to retain the high imaging speed of RSOM, while adding the information from multiple orientations. Currently linear arrays do not reach the frequency band utilized herein for achieving high-resolution imaging [26,27].

Advances in the sensitivity and bandwidth of linear arrays can further accelerate the acquisition speed of MORSOM[16].

In the future we will focus on enabling multicolor imaging[7] as well as faster scanning and reconstruction times. Finally, the combination of MORSOM with SPIM[30] in a single hybrid modality , or with other optical microscopic imaging modalities[19], this will give complimentary contrast, and complimentary imaging performance at different scales.

Acknowledgements

We thank Laura Pola Morell for help with the zebrafish, we also thank Andrei Chekkoury for valuable comments, we thank Dominik Soliman for help with measuring the impulse response of the detectors. V.N. acknowledges financial support from the Bundesministerium für Bildung und Forschung (BMBF), Bonn, Germany (Project "Tech2See", 13N12624).

Competing financial interests

V.N. has a financial interest in iThera Medical GmbH, which, however, did not support this work. K.W., T.S.-M. and T.M. work for the ZEISS group, who is a manufacturer of optical microscopes.

References

1 Barbosa, J. *et al.* Live imaging of adult neural stem cell behavior in the intact and injured zebrafish brain. *Science* **348**, 789-793 (2015).

2 Schönbauer, C. *et al.* Spalt mediates an evolutionarily conserved switch to fibrillar muscle fate in insects. *Nature* **479**, 406-409 (2011).

3 J. Huisken, J. Swoger, F. Del Bene, J. Wittbrodt & Stelzer, E. Optical Sectioning Deep Inside Live Embryos by Selective Plane Illumination Microscopy. *Science* **305**, 1007-1009 (2004).

4 Ntziachristos, V. Going deeper than microscopy: the optical imaging frontier in biology. *Nature Methods* **7**, 603-614 (2010).
5 P. Mahou *et al.* Multicolor two-photon tissue imaging by wavelength mixing. *Nature Methods* **9**, 815-818 (2012).
6 Zhu, L., Li, L., Gao, L. & Wang, L. V. Multiview optical resolution photoacoustic microscopy. *Optica* **1**, 217-222 (2014).
7 D. Razansky *et al.* Multispectral opto-acoustic tomography of deep-seated fluorescent proteins in vivo. *Nature Photonics* **3**, 412-416 (2009).
8 Omar, M., Gateau, J. & Ntziachristos, V. Raster-scan optoacoustic mesoscopy in the 25-125 MHz range. *Opt Lett* **38**, 2472-2474, doi:10.1364/OL.38.002472 (2013).
9 Omar, M., Soliman, D., Gateau, J. & Ntziachristos, V. Ultrawideband reflection-mode optoacoustic mesoscopy. *Optics Letters* **39**, 3911-3914 (2014).
10 Omar, M., Schwarz, M., Soliman, D., Symvoulidis, P. & Ntziachristos, V. Pushing the Optical Imaging Limits of Cancer with Multi-Frequency-Band Raster-Scan Optoacoustic Mesoscopy (RSOM). *Neoplasia* **17**, 208-214 (2015).
11 Tzoumas, S. *et al.* Immune cell imaging using multi-spectral optoacoustic tomography. *Opt Lett* **39**, 3523-3526, doi:10.1364/OL.39.003523 (2014).
12 Wang, L. V. & Hu, S. Photoacoustic tomography: in vivo imaging from organelles to organs. *Science* **335**, 1458-1462 (2012).
13 Beard, P. Biomedical photoacoustic imaging. *Interface Focus* **1**, 602-631 (2011).
14 Gamelin, J. *et al.* Curved array photoacoustic tomographic system for small animal imaging. *Journal of biomedical optics* **13**, 024007-024007-024010 (2008).
15 J. Gateau, A. Chekkoury & Ntziachristos, V. High-resolution optoacoustic mesoscopy with a 24 MHz multidetector translate-rotate scanner. *Journal of Biomedical Optics* **18**, 106005 (2013).
16 Li, G., Li, L., Zhu, L., Xia, J. & Wang, L. V. Multiview Hilbert transformation for full-view photoacoustic computed tomography using a linear array. *Journal of biomedical optics* **20**, 066010-066010 (2015).
17 Huisken, J. & Stainier, D. Y. Even fluorescence excitation by multidirectional selective plane illumination microscopy (mSPIM). *Optics letters* **32**, 2608-2610 (2007).
18 G.J. Tserevelakis, D. Soliman, M. Omar & Ntziachristos, V. Hybrid Multi-photon and Optoacoustic Microscope. *Optics Letters* **39** (2014).
19 Soliman, D., Tserevelakis, G. J., Omar, M. & Ntziachristos, V. Combining microscopy with mesoscopy using optical and optoacoustic label-free modes. *Scientific reports* **5** (2015).
20 P. M. Flood, R. Kelly, L. Gutiérrez-Heredia & Reynaud, E. G. Zeiss Lightsheet Z.1 Sample preparation. (Carl Zeiss Microscopy GmbH, Jena, Germany, 2013).
21 Yaroslavsky, L. P. & Caulfield, H. J. Deconvolution of multiple images of the same object. *Applied optics* **33**, 2157-2162 (1994).
22 Gustafsson, M. G. *et al.* Three-dimensional resolution doubling in wide-field fluorescence microscopy by structured illumination. *Biophysical journal* **94**, 4957-4970 (2008).
23 Zhang, C. *Submicron-resolution Photoacoustic Microscopy of Endogenous Light-absorbing Biomolecules* Doctor of Philosophy thesis, Washington University in St. Louis, (2014).
24 Cobbold, R. S. *Foundations of biomedical ultrasound*. (Oxford University Press, USA, 2007).
25 Kelsh, R. N. *et al.* Zebrafish pigmentation mutations and the processes of neural crest development. *Development* **123**, 369-389 (1996).
26 Chekkoury, A. *et al.* Optical mesoscopy without the scatter: broadband multispectral optoacoustic mesoscopy. *Biomedical Optics Express* **6**, 3134-3148 (2015).

27 J. Gateau, A. Chekkoury & Ntziachristos, V. Ultra-wideband three-dimensional optoacoustic tomography. *Optics Letters* **38**, 4671-4674 (2013).
28 J. Gateau, MA Araque Caballero, A. Dima & Ntziachristos, V. Three-dimensional optoacosutic tomography using a conventional ultrasound linear detector array: whole-body tomographic system for small animals. *Medical Physics* **40** (2013).
29 Chitnis, P. V. *et al.* Coherence-Weighted Synthetic Focusing Applied to Photoacoustic Imaging Using a High-Frequency Annular-Array Transducer. *Ultrasonic imaging*, 0161734615583981 (2015).
30 Lin, H.-C. A. *et al.* Selective plane illumination optical and optoacoustic microscopy postembryonic imaging. *Laser and Photonics Reviews* (2015).

Figures

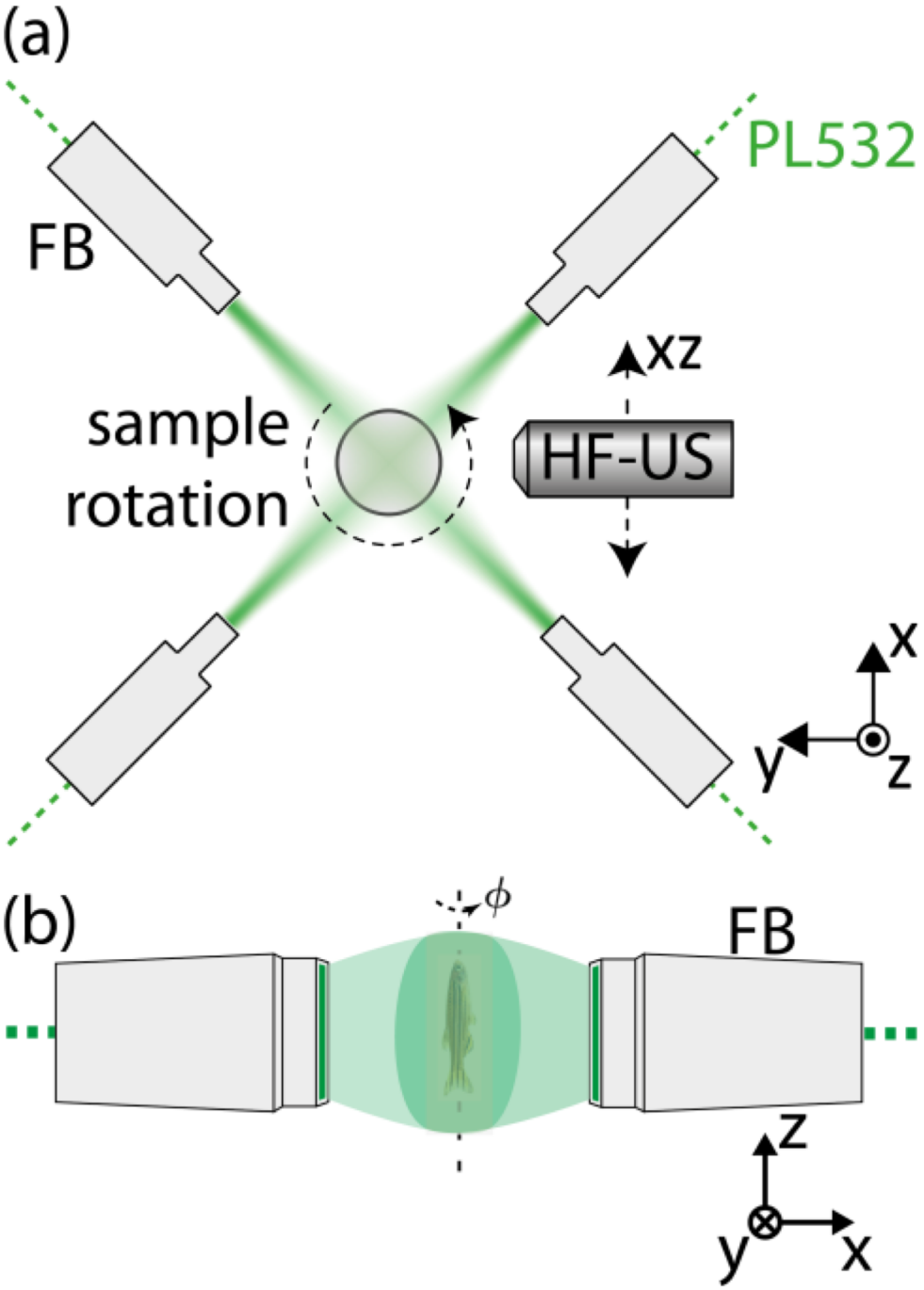

Figure 1: (a)Top view of the system, showing the configuration of the fiber bundles, the location of the ultrasound detector, the scanning the xz-plane, and the rotation around the z-axis, (b) side view of the system, showing the sample orientation, and illumination..

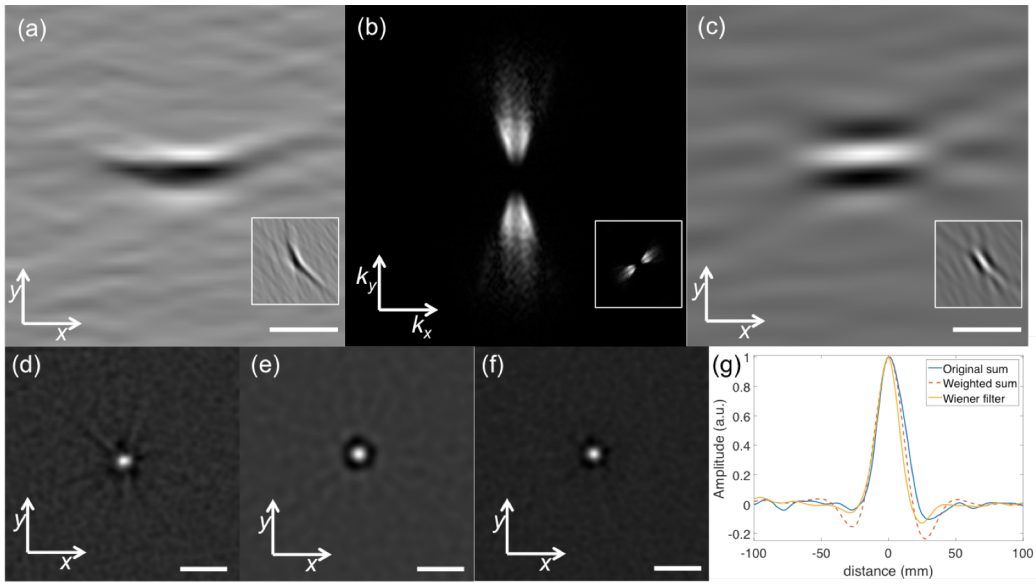

Figure 2: (a) point spread function (PSF) of an RSOM projection in the xy-plane at the angle 0°, inset shows the PSF at 60°, (b) magnitude of the optical transfer function (OTF) of RSOM at 0°, and at 60° in the inset, (c) an image of a sphere corrected with the OTF in the frequency domain at 0°, and 60° in the inset, (d) multi-view reconstruction of a microsphere, (e) multi-view reconstruction using a weighted sum, (f) multi-view reconstruction using weighted sum, and Wiener filtering, (g) Cross sections through the reconstruction *d-f*. (Scale bars: 100 µm)

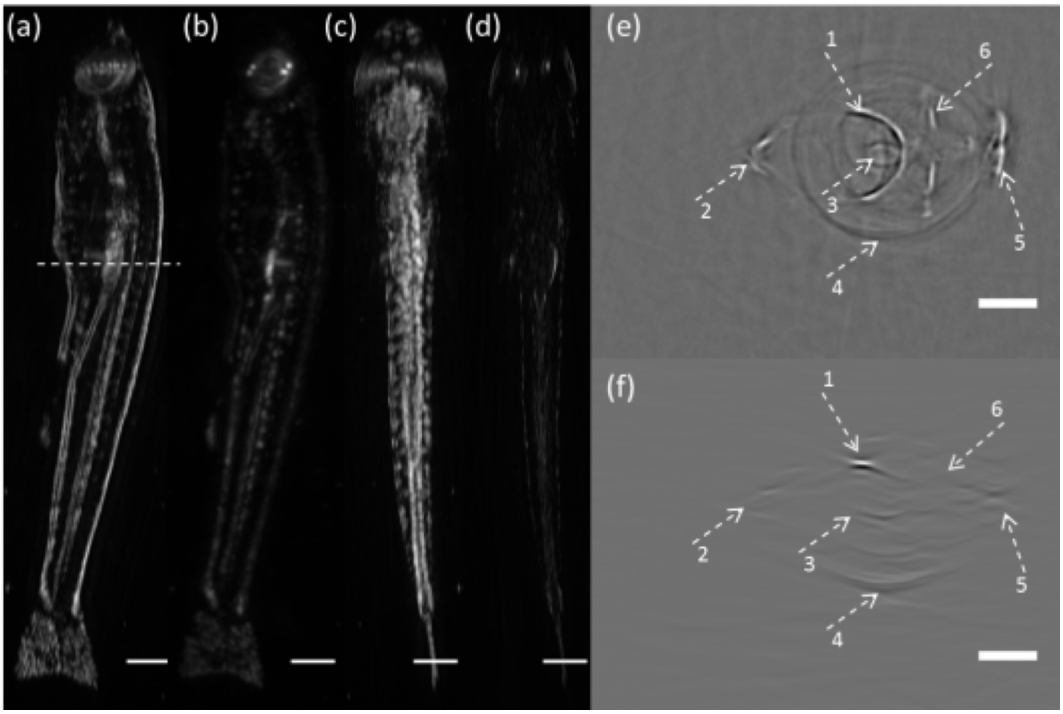

Figure 3: Comparison of the images generated using MORSOM, and RSOM. (a) Top view MIP from MORSOM, (b) top view MIP from RSOM, (c) side view MIP from MORSOM, (d) side view MIP from RSOM, (e) cross section through the zebrafish, taken from MORSOM at the position indicated by the broken line in Fig.3a, (f) same cross section from RSOM. The arrows point to similar features between Fig.3e and Fig.3f, in the MORSOM case many features are either complete, or do not even appear on Fig.3f (Scale bars: a-d: 500 µm, e,f: 250 µm, 0.3% of the pixels in a-d were saturated to improve visibility of RSOM images.)

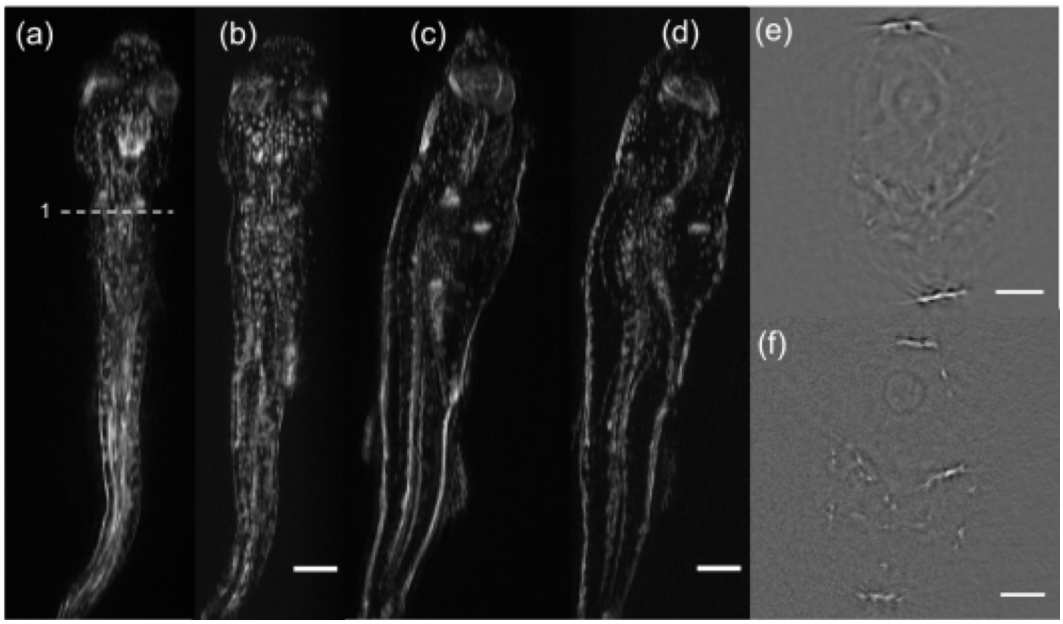

Figure 4: Comparison of MORSOM at 50 MHz and at 100 MHz. (a) Side view MIP from MORSOM at 50 MHz, (b) Side view MIP from 100 MHz, (c) top view MIP from 50 MHz data, (d) top view MIP from 100 MHz data, (e) cross section through the zebrafish at 50 MHz compared with one at (f) 100 MHz. (Scale bars: a-d: 500 µm, e,f: 250 µm)